Review

Hard X-ray and Soft Gamma Ray Polarimetry with CdTe/CZT Spectro-Imager

Ezio Caroli [1],* [ID]**, Miguel Moita [2], Rui M. Curado da Silva [2]** [ID]**, Stefano Del Sordo [3], Giovanni de Cesare [1], Jorge M. Maia [2,4] and Marcela Pàscoa [2]**

[1] INAF/OAS di Bologna, I-40129 Bologna, Italy; giovanni.decesare@inaf.it
[2] LIP-Coimbra, Departamento de Física da Universidade de Coimbra, Rua Larga,
    P-3004-516 Coimbra, Portugal; miguel.moita@coimbra.lip.pt (M.M.);
    rui.silva@coimbra.lip.pt (R.M.C.d.S.); jmaia@ubi.pt (J.M.M.); marcelapascoa@hotmail.com (M.P.)
[3] INAF/IASF-Palermo, I-90146 Palermo, Italy; stefano.delsordo@inaf.it
[4] Departamento de Física, University of Beira-Interior, P-6201-001 Covilhã, Portugal
* Correspondence: ezio.caroli@inaf.it; Tel.: +39-051-639-8678

check for updates

Abstract: CdTe/CZT based spectroscopic two-dimensional (2D)/three-dimensional (3D) imagers when operated in the Compton regime can work as high performance scattering polarimeters, for high-energy astrophysics. Polarimetry in high-energy astrophysics has been little explored. To date, X- and γ-ray source emissions have been studied almost exclusively through spectral, imaging, and timing analysis. Polarization measurements provide two additional observational parameters: the polarization angle and the level of linear polarization. These additional parameters should allow for a better discrimination between the physical mechanisms of different emission models characterizing a celestial object. Therefore, polarimetry will play a strategic role in new instrumentations for future high-energy astronomy missions. 2D and 3D CZT/CdTe spectroscopic imagers provided with coincidence readout logic can efficiently handle scattering events to perform simultaneously polarization, spectroscopy, imaging, and timing measurements. Herein, we describe the results obtained, both experimentally and by MC simulations, with CdTe/CZT pixel detector prototypes in high-energy polarimetry. We give an overview on the achievable polarimetric performance with spectroscopic imagers and on how these performances are affected by detector configuration parameters. Finally, we address the perspective of scattering polarimetry opened by the recent implementation of new high energy focusing optics, as broadband Laue lens, in next generation of hard X- and soft γ-ray astronomy instrumentation. The unprecedented sensitivity achievable by these telescopes will definitely open the window of polarimetry in this high-energy range.

Keywords: scattering polarimetry; CdTe/CZT spectrometers; pixel detectors; X- and γ-rays astrophysics

1. Introduction

High-energy polarized emissions are expected in a wide variety of γ-ray sources, such as pulsars, solar flares, active galactic nuclei, galactic black holes, and gamma-ray bursts [1–3], but polarimetry in this energy regime is an almost unexplored field mainly due to two facts. In the first place, the expected polarized portion of hard X/γ-rays flux from cosmic sources is in general only a small percentage of the already low incoming flux (few % to 10–20%), and only in few cases can represent a large fraction of it (>40%), requiring an instrument with very high sensitivity to be detected. Second, X/γ ray polarimetric measurements require the implementation of the complex of detection, electronic, and signal processing systems, on-board to high-altitude balloon or satellite missions in space. Therefore, until few years ago, no dedicated hard X/γ-ray polarimetric mission have been launched into space,

and X- and γ-ray source emissions have been studied almost exclusively through spectral, timing, and analysis of the measured fluxes and by using imaging techniques. On the other hand, polarization measurements will increase the number of observational parameters of a γ-ray source by two: the polarization angle and the level of linear polarization. These additional parameters should allow for a better discrimination between different emission models characterizing the same object. Polarimetry observations can provide important information about the geometry of the emission region, the intensity of the magnetic field, and other important parameters of the emission mechanisms. Up to now, in the soft γ-ray domain (0.1–1 MeV), only a small number of polarimetric measurements were performed by space instruments. SPI and IBIS instruments on-board the INTEGRAL (INTErnational Gamma-Ray Astrophysics Laboratory) mission [4], have reported statistically significant polarization observations on the Crab Pulsar, on the galactic black hole Cygnus X-1, and on some high flux gamma-ray bursts (GRB) [5–8]. On GRB's other results on the same energy range have been reported by the GAP (GAmma-ray burst Polarimeter) instrument operating on the IKAROS satellite [9], and more recently by observations of the ASTROSAT CZT-Imager (100 to 300 keV) [10]. Furthermore, new polarization measurements on the Crab source have been obtained by the same CZT-Imager [11] and by the balloon borne payload PoGO+ (20 to 160 keV) [12].

Today, the importance of high-energy polarimetry is largely recognized, and several research groups are involved in the development of dedicated instruments [13–15]. In any case, the next generation of space telescopes should provide polarimetric measurements, contemporaneously with spectroscopy, timing, and imaging. These multi-purpose instruments were proposed in recent high-energy (100 keV–1 GeV) space mission concepts submitted to ESA Cosmic Vision calls, such as GRI (Gamma-Ray Imager), DUAL, and e-ASTROGAM [16–18].

Since year 2000, our group proposed the use of pixel detectors as scattering polarimeter in the hard X- and γ-ray domain [19]. A spatially segmented spectrometer inherently offers the possibility to operate as scattering (Compton) polarimeter, if equipped with a readout logic that allows for managing events with two (double events) or more (multiple events) interactions in coincidence (Figure 1). Furthermore, a polarimeter based on a pixel/voxel detector permits the optimal use of the entire sensitive volume, since each element operates at the same time as a scatterer and as an absorber one. A straightforward advantage in using segmented detector, such two-dimensional (2D)/three-dimensional (3D) spectro-imager, as Compton polarimeter has the capability to perform contemporary spectroscopy, timing, and imaging measurements. This capability allows for overcoming problems that are linked to the inherent time variability of both cosmic sources flux and instrumental background, allowing for a direct correlation between the various types of measurement for the same observation.
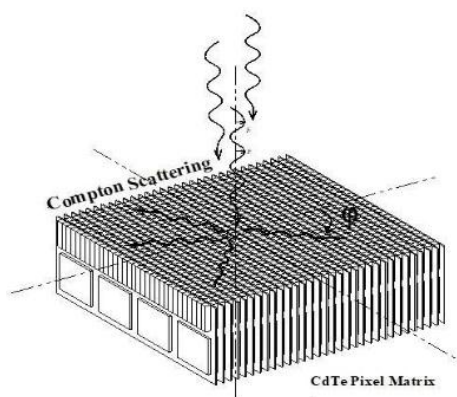

Figure 1. A schematic of a CdTe/CZT segmented spectrometer. The impinging photons can be scattered inside the same sensitive volume. The possibility to determine the interaction position and the energy deposit of photons that hit one of detector sensitive unit and scatter inside a different one allow for measuring the polarization status (i.e., direction and fraction) of the impinging photons.

The choice of CZT/CdTe [20] spectroscopic imager as scattering polarimeter, allows for optimizing the detection efficiency, due to the high atomic number of the material, and simultaneously ensuring good spectroscopic performance and high spatial resolution (2D or 3D). Obviously, this implies a limitation on the low energy threshold useful for polarimetric measurement. In fact, in these materials, the Compton cross section becomes significant only above 100 keV, by equating the photoelectric one approximately at 200 keV, and so a CZT/CdTe spectro-imagers can work efficiently as scattering polarimeters above 100 keV and depending on the thickness up to energies of the MeV region.

Herein, we give a summary of the results that were obtained by our group in studying the performance of CdTe/CZT segmented detector used as scattering polarimeters in the hard X- and soft γ-ray regime, as well as some perspectives in their use as focal plane in a next generation of high sensitivity space instruments.

2. Scattering Polarimetry Basic Principles

The polarimetric performance of a high-energy detection plane is determined by the fundamental concepts that are associated with polarized Compton interactions and by its design. The Compton scattering of a polarized photon beam generates non-uniformity in the azimuthal angular distribution of the scattered photons. The scattered photon angular direction depends on its initial polarization angle. If the scattered photon goes through a new interaction inside the detector, the statistical distribution of photons angular directions defined by the two interactions (double-event) provides a modulation curve from which we can derive both the degree and the polarization direction of the incident beam. The azimuthal angular distribution of the scattered photons is given by the Klein-Nishina differential cross-section for linearly polarized photons:

$$\frac{d\sigma}{d\Omega} = r_0^2 \left(\frac{E'}{E} \right)^2 \left[\frac{E'}{E} + \frac{E}{E'} - 2\sin^2\theta \cos^2(\phi - \phi_0) \right] \tag{1}$$

where r_0 is the classical electron radius, E and E' are, respectively, the energies of the incoming and outgoing photons, θ the angle of the scattered photons, and ϕ is the azimuthal angle between the scattering plane (defined by the incoming and outgoing photon directions) and the incident polarization plane (defined by the polarization direction and the direction of the incoming photon), which azimuthal orientation respect to a fix reference system is given by ϕ_0. This last coefficient represents the so-called polarization phase. As can be seen from Equation (1), after fixing all of the other parameters, the scattering probability varies with the azimuthal angle ϕ and its maximum and minimum arises for orthogonal directions (Figure 2a). For $\phi = \phi_0$, the cross-section reaches a minimum and for $\phi = \phi_0 + 90°$ the cross-section reaches a maximum. However, this relative difference reaches a maximum for a scattering angle θ_M, which is dependent on the incident photon energy [1]. For hard X/γ-rays (0.1–1 MeV), the θ_M value is 90° at ∼100 keV slowly decreasing down to ∼75° at 1 MeV (Figure 2b). Note that E and E' are related through:

$$\frac{E'}{E} = \left[1 + \frac{E}{m_0 c^2} (1 - \cos\theta) \right]^{-1} \tag{2}$$

where c is the speed of light in free space and m_0 is the electron rest mass.

From the expression of Equation (1), the modulation of the polarization results in a periodic function of the scattering azimuthal angle ϕ with a half period of $\pi/2$, as shown in Figure 2c. The difference between the maximum and the minimum of these curves provide the maximum polarization degree of 100% linearly polarized photons after Compton scattering. The modulation curves shown in the figure represent those that would be seen by a continuous detector with infinitesimal spatial resolution.

A scattering polarimeter is an instrument that can measure the modulation that is induced by the incoming photon polarization in the Compton scattering azimuthal distribution. A useful parameter

to evaluate the performance as scattering polarimeter is the so called modulation factor, Q_{100}, which gives a measure of how the detector see the modulation in the double-event distribution generated by a 100% polarized beam. For the case of a planar pixelated detector, Q_{100} can be calculated from the double-event angular distribution around a central irradiated pixel:

$$Q_{100} = \frac{N_{\max} - N_{\min}}{N_{\max} + N_{\min}};$$

(3)

where $N_{\max}$ and $N_{\min}$, are the number of double-events integrated over the two orthogonal directions defined on the detector plane along the maxima and minima of the scattered event distribution [21], corresponding in Equation (1) to $\phi = \phi_0 + 90°$ and $\phi = \phi_0$, respectively.
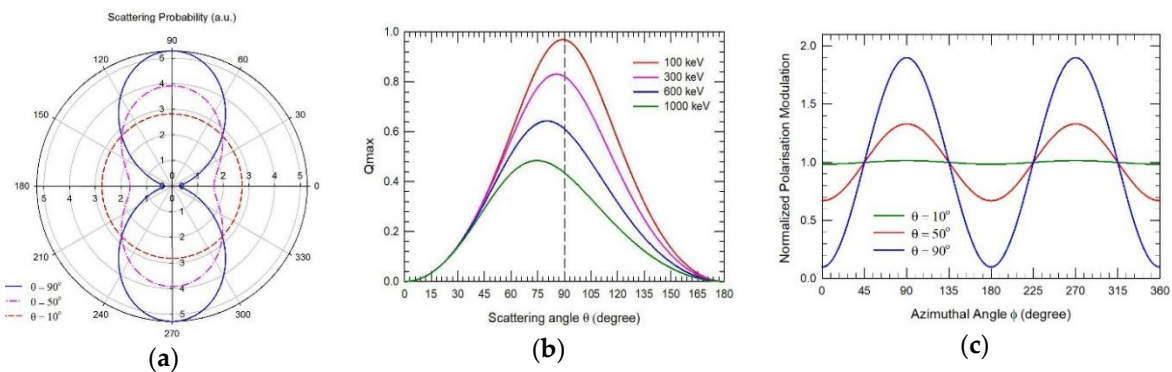

Figure 2. (**a**) The polar plot of the angular distribution in the azimuthal angle for a 200 keV 100% linearly polarized beam undergoing Compton scattering. The shape of this distribution strongly depends on the scattering angle, with a modulation that becomes more and more evident for scattering angles close to 90 degree; (**b**) The modulation curves corresponding to the polar plots in (**a**); for an easier comparison, the modulation curve have been normalized to their respective means; and, (**c**) The maximum modulation expected by 100% polarized photon beam as function of the scattering angle for various energies.

In practice, the Q_{100} of an $n \times n$ pixels' spectrometer used as polarimeter is calculated by a two-step procedure. The first step is to create the so-called scattering maps of the recorded Compton events. These map arrays have up to twice the dimension of the detector pixel array. For each Compton scattered event, the corresponding pixel of one the two hits is used as reference for the second one, which is added to the cell corresponding to its relative position in an array that has the same dimension of the pixel detector. At the end, each scattering map cell counts the number of Compton events that have the same azimuthal scattering angle, whatever the photon incidence point is. Therefore, the scattering map provides a direct representation of how the detector see the azimuthal dependence of the Compton scattering for polarized photons (Figure 2a), however it does not represents the real distribution of the counts inside the detector. The second step is the construction of the modulation curve, i.e., the curve that provides the number of scattered counts as a function of the azimuthal angle. This curve allows for evaluating both the modulation factor Q and the polarization phase, which is the direction of the polarization plane with respect to reference system, such as the one defined by the side axis of the detector. This curve is built dividing the scattering map on a fixed number of angular sectors to cover 360° and integrating, eventually after the application of event selection criteria (e.g., scattering distance range, energy window, etc.), the counts inside each angular sectors.

The aperture of the angular sectors should be chosen taking into account the discretization level of the detector (i.e., the pixel dimensions) and the double counts statistics. Because of the segmented nature of the detector, the integration of count inside a defined angular sector should take into account effects due to pixels that lie across their borders. Methods to account for these pixels are, for example, that of distributing the pixel counts proportionally to the area of the pixel intercepted by two adjacent

angular sectors. This division can be simply analytic or performed by means of a uniform random distribution of the counts, or still being determined using a Monte Carlo simulation on a realistic model of the detector. Examples of both measured scattering maps and reconstructed modulation curve are given later in Section 4. Once the modulation curve is built, the *Q* factor is evaluated directly from the difference between counts at angle ϕ, corresponding to the maximum and at $\phi + \pi/2$, normalized by their sum, as expressed in Equation (3).

For a given polarimeter, another parameter is of fundamental importance to quantify its final performance, once implemented in a particular instrument: the Minimum Detectable polarization (MDP). MDP gives a measure of the confidence that polarization is detected: if the reconstructed polarization fraction is equal to MDP, then there is only a 1% probability that it is resulting from statistical fluctuations of an unpolarized flux. The expected MDP should be significantly smaller than the degree of polarization to be measured. For a space polarimeter in a background noise environment, the following relation estimates the MDP at the 99% confidence level [22]:

$$MDP_{99\%} = \frac{4.29}{A \cdot \varepsilon \cdot S_F \cdot Q_{100}} \sqrt{\frac{A \cdot \varepsilon \cdot S_F + B}{\Delta T}}; \tag{4}$$

where Q_{100} is the modulation factor for a 100% polarized source, ε the double event detection efficiency, *A* the polarimeter detection area in cm^2, S_F the source flux (photons/s/cm^2), *B* is the background count rate (counts/s), and ΔT the observation time in seconds.

3. Hard-X and Soft γ-rays Polarimetry with 2d/3d Segmented CZT/CdTe Spectrometers

The development of CZT/CdTe spectrometers with high 2D/3D spatial resolution and fine spectroscopy represent a challenge to the realization of a new class of high performance instruments, for hard X/γ-rays, which are able to fulfil the current and future requirements in several applications fields.

Furthermore, 3D CZT/CdTe spectro-imagers, because their high spectroscopic resolution, (few % FWHM at 60 keV and <1% above 600 keV) and the high 3D spatial resolution (0.2–0.5 mm) achievable, allow for operating not only in full energy mode, but also as Compton scattering detectors if equipped with an appropriate electronics providing a suitable coincidence logic to handle multi-hit events. Because of these possibilities, such sensors are suitable to realize wide field detector for γ-ray sources (>100 keV) localization and detection, both in ground and space applications. Evaluation done using a single thick 3D CZT sensor as a 4π Compton Imager has demonstrated the possibility of obtaining an angular resolution of 15 degrees at 662 keV [23]. This is really an excellent result in the small distance scale used to reconstruct the Compton events kinematics and can be achieved only because of the good 3D and spectroscopic performance of the CZT proposed sensor units.

Performing a Compton scattering based polarimetric analysis requires an effective detection of Compton scattered photons and the inherent capability of the detector to detect the modulation of the scattering. The efficiency is given by nature for this kind of large volume 3D detector as Compton scattering is the dominant interaction for hard X- and soft γ-rays. The detector capability to operate as a polarimeter depends on the capability to detect the scattered photons and to select the interesting events (those with a scattering angle around 90 degrees show the strongest modulation). Both is given for our 3D detector; first, because of its high atomic number, the material acts as a good absorber: (a 1 MeV primary photon has an energy of only 338 keV after a scattering of 90°, which makes photoelectric absorption more probable). Second, because a good selection along the third coordinate (depth) can be made which allows for obtaining an optimized modulation curve, analyzing, for each layer of the virtual stack, the events with scattering angles that are close to 90 degrees.

In fact, a 3D spectrometer that is able to handle properly scattered events in three dimension over the entire sensitive volume can even offer better performance as scattering polarimeter. In the case of 3D spectrometer device, each single sensor unit could be operated as a small Compton polarimeter [24].

4. Scattering Polarimetry with CdTe/CZT Pixel Spectrometers: The PolCA Series Experiments

To assess and optimize the polarimetric performances of future hard X- and γ-rays space instruments, a series of experiments based on CZT/CdTe pixel detector prototypes were carried out using the ID 15 beam line at the European Synchrotron Radiation Facility (ESRF), where a ~99% linearly polarized X-ray beam is available [25–30]. The main purpose of these experiments, denominated as PolCA (POlarimetry with Cadmium Telluride Arrays) series, was to evaluate the polarimetric performance of CZT/CdTe pixel (2D) detectors up to 750 keV. Monte Carlo simulations were developed in parallel, implementing in the code the same CZT/CdTe detector prototype design irradiated under analogous conditions. The Monte Carlo simulation tools are based on the GEANT4 (GEometry ANd Tracking) environment [31]. The simulation code implemented two main functions: (a) the module that describe the physics of the electromagnetic interactions of polarized photons, in particular, for the Compton scattering; and, (b) the detection system with the definition of the beam characteristics, the detector geometry and materials, and the readout logic.

Several types of CZT/CdTe detectors (Eurorad, IMARAD, and ACRORAD) were tested under the PolCA experiment's series. Herein, we give a summary of the main results that were achieved with the last two pixel detector prototypes we used and for which we obtain the most significant results.

The first polarimeter detector was based on an IMARAD 5 mm thick CZT mosaic of four units with anodes that were segmented to obtain a total of 16×16 pixels, each with 2.5×2.5 mm^2 area. Due to limitations in our back-end electronics (only 128 channels available), only 11×11 pixels have been connected for a total sensitive area of ~8 cm^2. The CZT unit was installed on a supporting layer that contains the height 16 channel ASIC's [32], the bias circuit, and the connectors for the back-end electronics (Figure 3a). This front-end electronics were read by a 128 channels multi-parametric system that handle both the coincidence logic and provide to build the events data stream that is stored in a 32 bits parallel words files [26].

The second pixel device we report about is the Caliste-256 Module [33], which was developed at CEA, started in the framework of a french-italian space mission proposal [34]. This space qualified device (Figure 3b) is a high performance pixel spectrometer with a fine pitch (0.580 mm) that can be equipped with two different sensor type of 1 cm^2 sensitive area: 1 mm thick Schottky CdTe and 2 mm thick CZT. The sensor is coupled to a four-buttable integrated front end electronics implementing 8 full custom ASICs IDeF-X that are 32 channels chip providing the spectroscopic readout of the pixels [35]. This detector module is able to detect photons between 2 keV and 280 keV with 1 keV (FWHM) energy resolution at 60 keV.

A summary of the main characteristics of these two 2D spectrometers is given in Table 1. For all the reported test results on both detectors, we set a coincidence window of 10 μs to acquire the scattered events produced by the impinging photons.
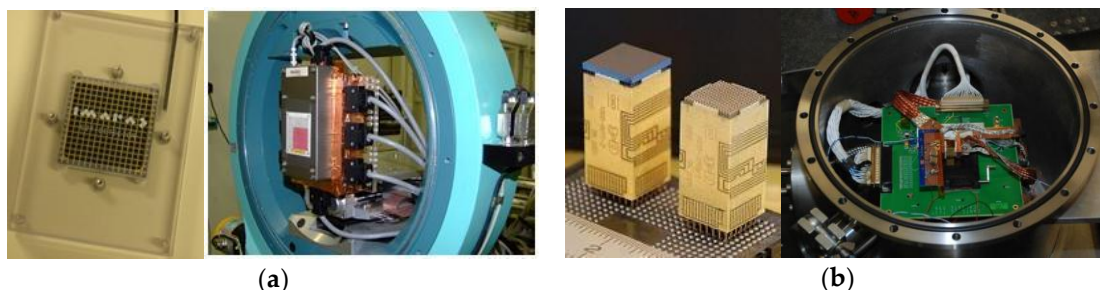

(a)　　　　　　　　　　　　　　　　　　　(b)

Figure 3. The pixel prototype used for the PolCA experiments at European Synchrotron Radiation Facility (ESRF) (ID15A): (**a**) The IMARAD two-dimensional (2D) CZT sensor (left), the PolCA-IMARAD detection system at the beamline inside its room temperature light tight container (right); and, (**b**) The Caliste-256 Module with the 1 mm thick Schottky CdTe (right), and the Caliste module mounted on its electrical and mechanical interface inside the thermo-vacuum container ($T \sim -10$ °C).

Table 1. Summary of the main characteristics of the two pixels CZT/CdTe detectors used in recent PolCA experiments.

	IMARAD-PolCA	Caliste PolCA
Material	CZT	CdTe Schottky and CZT
Sensitive area (cm^2)	2.75×2.75 over 11×11	0.93×0.93
Thickness (mm)	5	1 and 2
Pixel pitch (mm^2)	2.5×2.5	0.580×0.580
Pixel array	11×11 active over 16×16	16×16
Low energy threshold (keV)	30	2–3
Energy resolution, FWHM	6% at 122 keV	1% at 60 keV

4.1. The IMARAD-PolCA Polarimetric Tests

During several test sessions at ESRF (ID15A/B), we had the possibility to evaluate the behaviour as scattering polarimeter of the IMARAD-PolCA pixel detector in a wide energy range (100–500 keV) and in various geometrical irradiating configurations.

The pixel size of the IMARAD PolCA determine the polarimetric response, i.e., its sensitivity to the azimuthal modulation of the scattering induced by the photon beam polarization, of such detector as shown in Figure 4, where the effect of its coarse segmentation is clearly visible in scattering maps. We should mention that the scattering maps have been obtained after correcting the non-uniformity in the pixel detection efficiency evaluated by using single events response scanning over each pixel of the detector for the same fixed time period. Furthermore, in the case of ESRF measurements in which the beam is collimated on the central pixel, the scattering maps give a direct representation of the real distribution of scattered photons inside the detector.
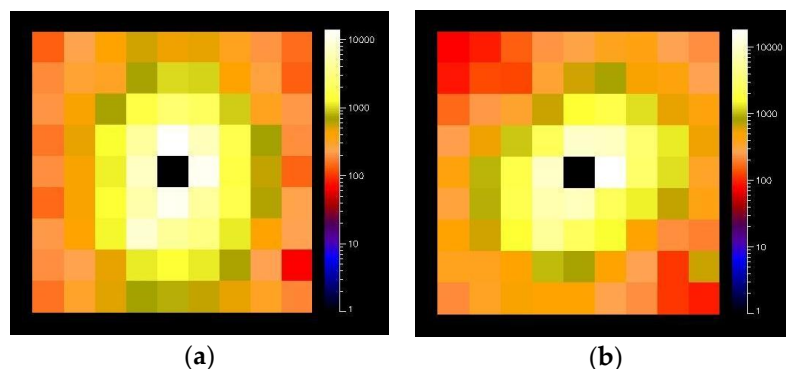

(**a**)　　　　　　　　　(**b**)

Figure 4. False color scattering maps obtained with the IMARAD-PolCA detector using a 511 keV beam at ESRF (ID15A) with two different orientation angle (ϕ_0) of the polarization plane with respect to the detector side axis: (**a**) $\phi_0 = 0°$; (**b**) $\phi_0 = 45°$. The photon beam was collimated at 0.5×0.5 mm^2 in the center of the central pixel, orthogonally to the detector plane. The central map cell is set black because represent only the reference point of each Compton scattered event and in the ESRF irradiation condition coincide with the impinging pixel.

The pixel size of the IMARAD PolCA determine the polarimetric response, i.e., its sensitivity to the azimuthal modulation of the scattering induced by the photon beam polarization, of such detector, as shown in Figure 4, where the effect of its coarse segmentation is clearly visible in scattering maps. We should mention that the scattering maps have been obtained after correcting the non-uniformity in the pixel detection efficiency that was evaluated by using single events response scanning over each pixel of the detector for the same fixed time period. Furthermore, in the case of ESRF measurements in which the beam is collimated on the central pixel, the scattering maps give a direct representation of the real distribution of scattered photons inside the detector.

Figure 5 provides a summary of the results that we obtained with the IMARAD PolCA detection system during several test runs. Figure 5a shows the evaluated Q_{100} factor of the CdZnTe prototype as a function of the polarized photon beam energy. These results were obtained after the correction for non-uniformity in the response of the detector pixels, by normalizing the relative efficiency of each pixel, evaluated from the single full energy absorbed events distribution, to a reference values (e.g., the value of the pixel that exhibit the maximum count rate).
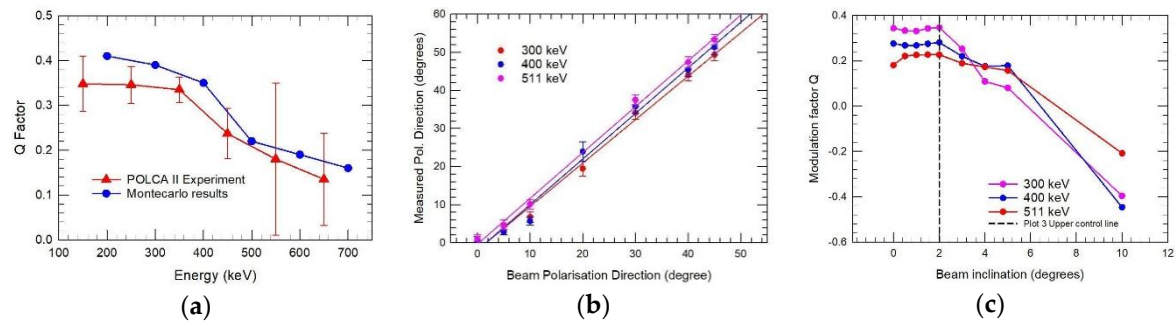

(a) (b) (c)

Figure 5. (**a**) The measured PolCA modulation Q_{100} factor (with 1 σ errors) as function of beam energy, compared with the results of a simple GEANT Monte Carlo model (the 1 σ errors are smaller than symbols); (**b**) The polarization plane direction reconstruction (with 1 σ errors) at different energies; and, (**c**) Systematic effect induced in the measure of the modulation factor Q_{100} by the zenithal inclination of the impinging photons.

For comparison, Monte Carlo simulations were performed of a 5 mm thick CdZnTe matrix similar to the PolCA prototype under analogous conditions and the results are shown on the same graph. The experimental modulation factor obtained is of ∼0.35 up to 350 keV. It decreases to ∼0.15 for 650 keV, since for higher energies the probability of Compton interactions occurring with a low scattering angle is higher than in the 150–350 keV band. The trend with energy of the IMARAD PolCA prototype performances is in good agreement with Monte Carlo results that are in fact always better than the measured ones. The discrepancy can be completely attributed to both the lower threshold and a better spectroscopic performance that is used in the numerical simulation with respect to the prototype operational conditions. From 550 keV to higher energies, a secondary synchrotron beam (due to a gap in the beam collimator shield) was projected onto the CdZnTe active surface, which introduced a substantial error component in the Q_{100} factor calculation.

Figure 5b gives the measured polarization direction angle as a function of the effective ESRF beam polarization angle at 300 keV, 400 keV, and 511 keV. The linear fits calculated for each energy are also represented. The measures are in good agreement with the effective beam polarization angle. The error bars of most of the measured polarization angles lie within a few degrees. The measured values exhibit larger uncertainties for angles near 45°. This is an expected result, since for these angles the pixels that correspond to the maximum and the minimum directions of the scattered event distribution lie close to the diagonal of the detector plane axis, where the effect due to square pixels is more pronounced.

Finally, the graph in Figure 5c shows the measured Q_{100} factor as a function of the tilt angle, i.e., the beam direction inclination with respect to the detector plane. We made these measurements having in mind that in space instrument for X and γ-ray astronomy the direction of the incoming radiation is not always perpendicular to the detector plane. This is particularly true for coded mask imaging systems that have a wide field of view, but it could be also true in the case of high energy focusing optics. The condition of non-perpendicularity between the incoming photons and the detector plane can affect the measurement of the polarization status, introducing systematics in the distribution of the scattered events. Up to 2° tilt angle, the Q_{100} factor is not significantly affected by the beam inclination. However, from 3° up to 10° tilt angles, the Q_{100} factor dramatically increases when polarization direction and inclination add their effects and decreases (as reported in the figure) when these effects

partially cancel each other. The change in sign of the Q_{100} means that for large tilt angles in the direction opposite to the polarization plane direction the scattering events distribution shape is really dominated by the photon incoming direction, which create an artifact modulation that correspond to a polarization plane direction opposite to the true one.

4.2. The Caliste-PolCA Polarimetric Tests

In May 2011, we succeed to perform a wide set of test using the Caliste 256 module as scattering polarimeter. The high performance in term of spectroscopy and response uniformity [33] in conjunction with the fine spatial resolution of the detector allowed for obtaining very precise and significant results on the achievable polarimetric performance of this kind of device.

For example, Figure 6 shows the scattering map for a 200 keV photon beam collimated at 50×50 μm impinging the centre of one of the central four pixels of the Caliste 256 module. The fine spatial resolution allow to see very well the "papillon" shape of the Compton scattering expected at this energy (Figure 2a). The well-defined shape of the scattering maps is reflected in the modulation curve that can be build. Figure 7a shows the modulation curve obtained by applying filters both on the scattering adjacency order, i.e., the distance in pixels between the two hits, of double events hits and on the double events energy to same events set used for the beside scattering map. In this graph, and in following ones, Q is defined as: $Q(\phi) = [N(\phi) - N(\phi + \pi/2)]/[N(\phi) + N(\phi + \pi/2)]$. Furthermore, we should point out that in the graph of modulation curve we did not report the counts integrated on each angular sector, but directly the correspondent modulation factor Q evaluated by Equation (3), and the change in sign is due to the exchange between the two terms in the numerator. The fact that the Monte Carlo errors are larger than the experimental ones is due to the lower count statistics that we used in the reported simulation with respect to the ESRF measurement at the same energy.
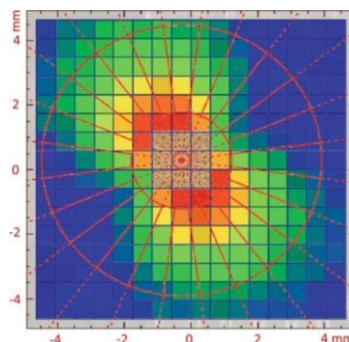

Figure 6. The false color scattering map with Caliste-256 for a 98% polarized 200 keV beam with the polarization plane 30° inclined with respect to the Caliste detector side axis. The red lines and circles show the the angular sectors and the double events hits distance range (adjacency order), respectively used to build the modulation curves presented in Figure 7.

In particular, the applied energy filter (139–148 keV) was equivalent to select event with scattering angles close to 90° that is the optimum value at 200 keV (Figure 2a). In the plots in Figures 7b and 8a,b are reported the results that were obtained with the CZT Caliste 256 module in term of sensitivity to the polarization plane direction. The Figure 7b shows the modulation curves built by integrating the counts in the scattering maps, as obtained by a 300 keV photon beam, in 15° wide angular sectors (areas between the red lines in Figure 6) for two close different orientation of the beam polarization plane with respect to the detector axis. The 10° degrees difference is well recognizable by the phase change in the two curves. In particular, Figure 8a demonstrated the high level of the linearity in the reconstruction of the polarization direction and its independence from energy between 200 and 300 keV. The two best-fit lines are very close to the $y = x$ direction, the small offset shown ($\sim -1°$) can be mainly attributed to both counts statistics and systematics (e.g., the effect of square pixel geometry). Finally,

Figure 8b reports the sensitivity in the measurable polarization fraction of the CZT Caliste module at 200 keV as compared with IMARAD PolCA results at 400 keV. This graph clearly shows that in the PolCA case the minimum detectable fraction is about 1.5 times larger than in the case of the Caliste detector (~38% with respect to ~27%). We chose to compare the IMARAD PolCA detector with respect to the Caliste module, using higher energies to take, at least partially, into account the effect of the difference in pixel sizes and energy thresholds between the two systems.
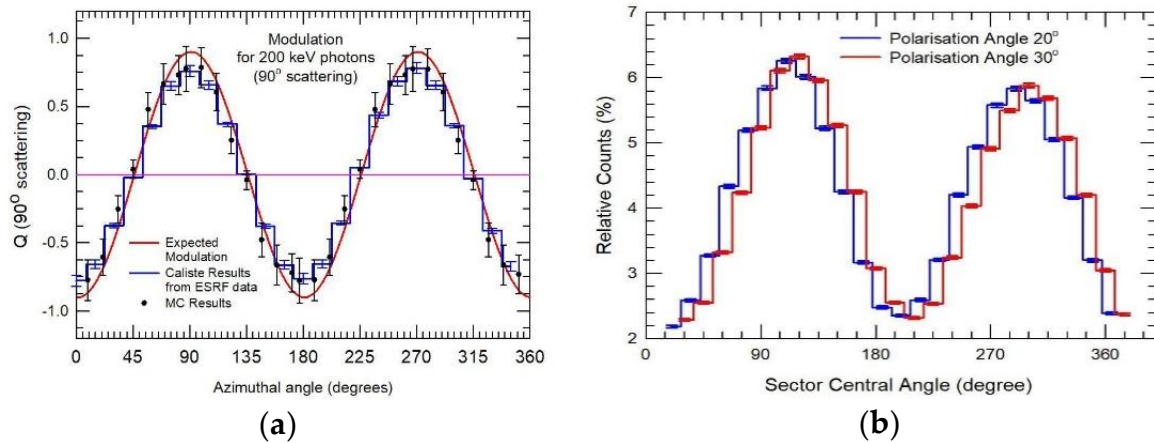

Figure 7. (**a**) The experimental Caliste modulation curve at 200 keV (blue line). The modulation factor Q_{100} measured with Caliste, applying the double events selection reported in the text, was ~0.78, i.e., very close to the theoretical expected values of 0.9 (red line). In black, the data obtained by the Caliste Monte Carlo model results are statistically consistent with the experimental results; and, (**b**) The modulation curve in term of relative counts in each angular sectors, with 1σ errors, obtained with CZT Caliste 256 at 300 keV (98% linearly polarized) for two different orientation (ϕ_0) of the polarization plane.
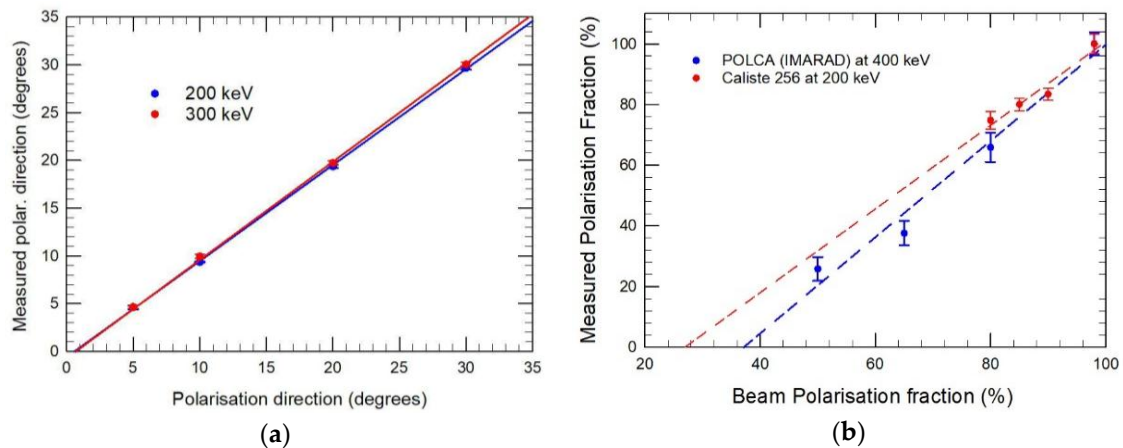

Figure 8. (**a**) The measured polarization plane direction versus the real beam polarization plane direction at two energies; and, (**b**) Comparison between the sensitivity to the beam polarization fraction evaluated from ESRF data for the PolCA (IMARAD) and the CZT Caliste 256 pixel detectors, respectively. The large difference between the two results is a confirmation of the modulation factor improvement achievable with a finest discretization (i.e., spatial resolution) coupled with fine spectroscopic performance.

The larger size of pixels (2.5 vs ~0.6 mm) and the higher energy threshold of the first detector with respect to the second one (~30 keV vs. 3 keV), drastically affect both the mean scattering path length and the scattered events statistics, i.e., the effective modulation factor. These effects are more evident

in the IMARAD PolCA detector for low energy. As shown, and, as expected, the Caliste 256 system is more efficient with respect to the IMARAD detector also in the reconstruction of the polarization fraction, allowing for measuring this parameter at least a factor of two better, i.e., Caliste can measure lower fraction of polarization with respect to the IMARAD detector.

5. 3D CZT Spectro-Imager as Scattering Polarimeters: A New Development Direction

The quality (modulation factor) of a scattering polarimeter strictly depends on both spatial and energy resolution, because these characteristics affect the capability of Compton kinematic reconstruction and thus good event selection, as shown in Section 4 [28,30]. Furthermore, in the development of new space instrumentations for hard X- and γ-rays astrophysics, the requirements to achieve high detection efficiency is almost mandatory. This implies, even when using high atomic number sensitive material, large thickness: for example, at 600 keV, a CZT detector should have several centimeters of thickness to guarantee more than 70% total detection efficiency. In this section, we focus on a particular type of CZT/CdTe segmented spectrometers that are able to provide a spatial resolution in three dimensions (i.e., 3D spectro-imagers). These devices represent the new frontiers for applications in different fields [36] that require increasing performance and are particularly promising for hard X- and soft γ-rays astrophysics instruments implementing new high energy focusing optics (see following Section 6) systems. In this context, such new generation of spectro-imagers will represent the required technological breakthrough to made polarimetry a standard operational observing mode, such as spectrometry and imaging, of the high-energy sky in the next decades. In the last 10–15 years, several groups have focused their activity on the development of 3D spectro-imager based on: (a) stacks of several thin (1–2 mm) CZT/CdTe high 2D spatial resolution layers [37]; and, (b) mosaic of large volume (1–10 cm^3) single CZT/CdTe crystals each capable of intrinsically operating as 3D spectrometer [38,39].

5.1. Monte Carlo Study of 3D Spectro-Imagers Polarimetric Performance

The precision with which the modulation, as produced by the polarization, can be determined depends on the scale of segmentation of the detector, that is, from its spatial resolution within its entire volume. For the same incident energy, the definition of the modulation depends on the number of angular bins that can be defined for a certain distance from the point of scattering (Figure 9a). Furthermore, we should point out that the spatial segmentation of a spectrometer, allowing for overcoming problems that are related with charge collection that are typical for CdTe/CZT sensors, provide, in general, better performance in terms of spectroscopy and response uniformity with respect to single planar electrodes sensors of the same sensitive volume.

Monte Carlo modelling represents an essential step in the optimisation of the polarimetric response of a 3D spectro-imager, and in the determination of the best trade-off between performance and detector design complexity.

We are using a simple GEANT4 numerical model to perform extensive simulation studies on the effect of different detector configuration parameters, such as the voxel dimension and the sensitive volume under various irradiation conditions (beam shape and spectrum) and the spectroscopic response model. The GEANT4 simulation are performed assuming a block of $20 \times 20 \times 2$ cm^3 as CZT detector sensitive volume. This volume can be segmented in 3D at any defined voxel size by a SW tool developed in MATLAB that read the event files generated by GEANT4 simulation runs [40]. Some results obtained for these two detector voxel segmentation scales are reported in Figure 9b,c, where the modulation curve have been expressed directly in term of modulation factor Q units (as in Figure 7a) instead of angular sector integrated counts. In the 3D case, the modulation curves are obtained with the procedure that is explained in Section 2, simply projecting the azimuthal angle simply onto the plane where the scattering occurs.
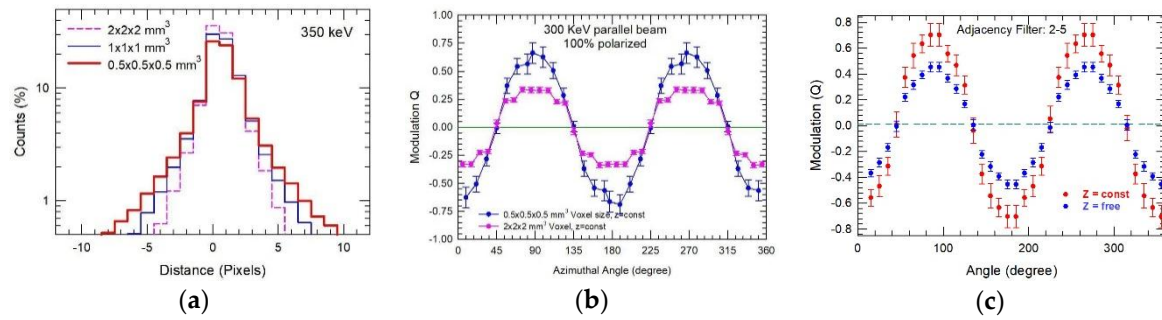
Figure 9. (**a**) The distribution of the distance in the XY plane (in pixel units) between the hits of Compton events as function of the sensitive volume discretization; (**b**) Modulation curve for two different discretization in voxel of the same sensitive volume obtained by selecting scattered events for which the two hits have the same coordinate in z (along the detector thickness); and, (**c**) Modulation curves obtained with voxel of $0.5 \times 0.5 \times 0.5$ mm^3 for a parallel monochromatic beam at 300 keV considering all the detected (blue) double events (z = free) and double events for which the two hits have the same coordinate in pixel units along the z-axis (z=const). In both cases, the double events are filtered considering only events with hits distances in the detector plane (i.e., adjacency) between two and five pixels.

Figure 9b reports the modulation curves that were obtained by irradiating the full CZT sensitive surface by a monochromatic (300 keV) and 100% polarized photon perpendicular beam and segmenting its volume in two quite different voxel scales: $2 \times 2 \times 2$ and $0.5 \times 0.5 \times 0.5$ mm^3. In both cases, the modulation curve have been obtained integrating the counts accumulated in the scattering map over 32 angular sectors with an aperture of $11.25°$ (i.e., covering 360 degrees) and selecting Compton events, which two hits have the same value of z (z = const) in pixel units. The improvement is well evident in the measured modulation of the fine voxel geometry with respect to the coarse one. With the fine voxel scale, the result is similar and statistically consistent to the one experimentally obtained with the Caliste module. Figure 9c compares the modulation curve that was obtained, using 36 ten degrees wide angular sectors, from the same MC data set analyzed by segmenting the sensitive CZT volume in the previous small scale voxels, and integrating all of the Compton's scattered events (z = free), i.e., equivalent to consider a 2D pixel detector, with the one built applying the filter z = const. The statistically significant difference in the maximum modulation between the two curves is mainly due to the selection of the most favorable scattering angles (around 90 degrees for 300 keV) to preserve the primary polarization information of the incident photons when selecting events with energy deposits having the same z coordinate, in practice on the same thin layer of detector. Furthermore, this figure demonstrates the importance of a thick detector (2 cm) to be segmented in three dimension inside is sensitive volume to be efficiently operated also as a scattering polarimeter. In the case of a 2D pixel thick detector, the response in polarimetry is made by the convolution over a large range of scattering angles with a significant loose in polarization modulation sensitivity (Q_{100} from $\sim$0.7 to $\sim$0.45).

5.2. The Compton-PolCA Experiment

In the perspective, to assess the achievable scattering polarimetric performance of a 3D spectro-imager, a new detection system configuration was developed and tested at the European Synchrotron Radiation Facility (ESRF) under ~99% linearly polarized X-ray beam. This configuration consists in a two layer Compton spectro-imager based on two CdTe pixel sensors, operated as a Compton scattering polarimeter (Figure 10). By varying the distance between the two CdTe pixel detection layers, it is possible to assess and study the scattering polarimetric performances of a multi-layer plane solution or equivalently of a 3D detector. These results will be relevant for the development of both high efficiency Laue lens telescope focal planes and all-sky advanced Compton telescope designs for the next generation of space missions.
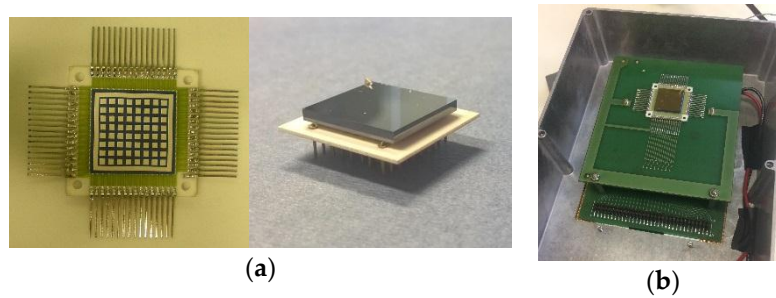
Figure 10. (**a**) The different bonding board of the top (left) and of the bottom CdTe pixel sensor (right) sensor of the Compton-PolCA detection system; and, (**b**) Picture of the detection system. Each PCB supports one of the detectors that are aligned in XY directions. The distance between the two detectors planes can be adjusted between 5 to 20 mm.

The detection system is based on two ACRORAD CdTe detectors both with 2.0 mm thick. Each detector matrix was divided into 8 × 8 pixels with an area of 1.9 mm × 1.9 mm each and with a 0.1 mm gap between consecutive pixels. The detectors were operated at room temperature with a bias voltage of 100 V (Table 2). The front and back-end electronics were the same as the previous PolCA experiments allowing for readout all the 128 pixels of the detection system.

Firstly, the two sensors of the prototype were measured individually to estimate both their response uniformity across each working pixels. The implemented coincidence logic allow for operating each single pixel sensor as an independent polarimeter and the two planes as another independent polarimeter by selecting the recorded double (i.e., scattered) events through the pixel address of the hits. In this experiment, we have the possibility to use a single monochromatic beam at 278 keV.

Table 2. Summary of the main characteristics of the Compton-PolCA Experiment.

Material	CdTe
Sensitive area/sensor (cm^2)	1.6 × 1.6
Thickness (mm)	2.0
Pixel pitch (mm^2)	2.0 × 2.0
Pixel array/sensor	8 × 8
Low energy threshold (keV)	40
Energy resolution, FWHM	8.3% at 278 keV

Using the two layers double events, we succeed to perform a preliminary evaluation of both the dependence with the distance between detectors of the modulation factor Q and its potential to determine the polarization angle orientation by performing measurements at different polarization direction angles. Regarding the potential to determine the polarization angle orientation the polarization angular resolution obtained was better that 9° (Figure 11a). As expected at this energy, the modulation factor Q decreases for increasing distances between detectors (Figure 9b). The reason for this result is that we deal with events with lower scattering angles accepted for higher distances, i.e., with events in which the scattering angle gets more and more away from the optimal condition (around 90°). In Figure 11b, the measured Q for two different distance between the pixels sensors are over plot with the theoretical estimate of the modulation factor Q at 300 keV for the full target distance range of the Compton-PolCA system. The two dashed curves have been obtained while weighing the expected modulation factor for 100% polarized 300 keV photons by the normalized scattering probability and integrating this product up the maximum scattering angle allowed by the geometrical parameters of the system (i.e., lateral size, pixel pitch and distance). Finally, the results were multiplied by two realistic value of the intrinsic modulation factor Q_{100} of the pixel sensors.
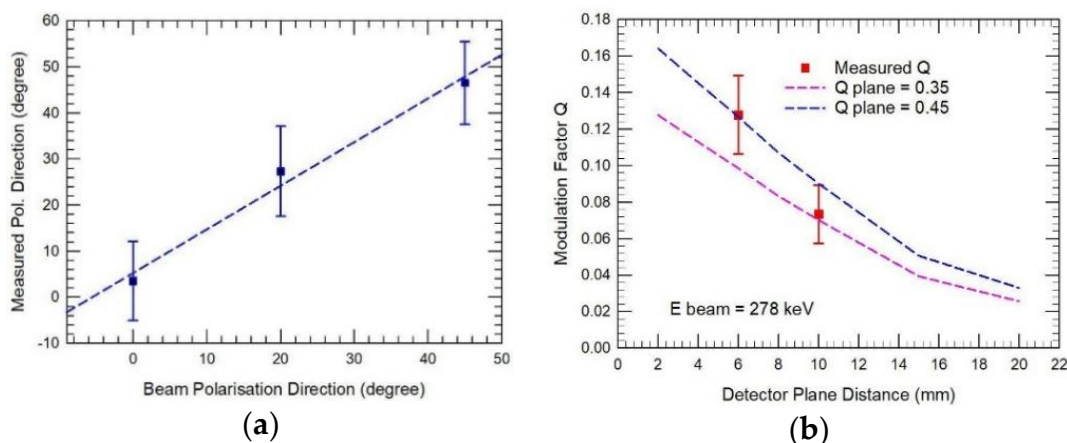
Figure 11. (**a**) Measured polarization plane direction for a 278 (99% polarized) keV beam as a function of the effective ESRF beam polarization angle; and, (**b**) The modulation factor Q_{100} measured for 278 keV photons at two different distances between the pixel detector planes (square symbols) as compared with an estimate of the expected modulation factor Q_{100} over the entire distance range of the Compton-PolCA system. The two dashed curves give the modulation factor Q expected for 300 keV polarized photons assuming two different realistic values for the intrinsic modulation factor Q_{100} of the detector pixel plane (Q plane).

6. Scattering Polarimetry: Perspective with New High Energy Focusing Telescope

With the advent of the NASA NuSTAR mission [41] having on board two focusing telescopes operating in the 3–79 keV band, very sensitive studies of the hard X-ray sky are finally becoming possible. However, in order to take full advantage of these developments, a new generation of focusing telescopes, which extend the energy band up to several hundred keV, is required. Besides high-resolution spectral and timing capabilities, these telescopes should also offer polarization determination capability.

In our understanding, a two order of magnitude increase in sensitivity, a strong improvement in both angular resolution and polarization functionality with respect to current instrument operating in the hard X- and soft γ-ray energy window will lead to a leap forward as, in a similar way that soft X-ray optics did in the 1970s. The Laue lens telescope, which is based on diffraction from crystals in a transmission configuration, offers a very interesting technical solution to the implementation of a focusing telescope that can extend the energy band beyond 80 keV.

Recently, an Italian collaboration has start developing broadband Laue lens capable to focus radiation in the wide energy pass-band 90–300 keV [42]. For the first time, crystals with bent crystallographic structure were used [43]. These bent crystals allow a wider energy passband and a reduced the point spread function (PSF) if compared with flat mosaic crystals: few square mm with respect to few square centimeters. Using this technology, it is possible to build broadband Laue lens telescopes, which main characteristics are fully compatible with a class M satellite mission as the one foreseen in the ESA Cosmic Vision 2015–2025 program. The sensitivity that such a telescope, with 20 m focal length and operating in the 70–700 keV range, can achieve is about 1000 better that the current instruments [44]. This type of high-energy optics impose very demanding and challenging requirements on focal plane detectors that should provide:

- good imaging capability with a 2D spatial resolution <0.5 mm;
- good spectral resolution ~1% at 500 keV;
- small sensitive area: ~25 cm^2; and,
- high detection efficiency: i.e., >80% up to 600/700 keV.

The first requirement depends on the expected size of the telescopes PSF. In fact, in order to guarantee the correct PSF sampling, the spatial resolution of the focal plane detector shall be smaller than the PSF; an oversampling by a factor of three is typically used. Such a fine-pitched sampling will also completely fulfill the requirement that is imposed by the expected angular resolution to discriminate the positions of two sources at 20 arcsec distance in the FOV.

The level of spectral resolution is important for several reasons. Good spectral resolution is necessary to perform a correct reconstruction of the photon source spectrum and to be able to have a good signal to noise ratio (SNR) in the detection of both emission and absorption line features in the source flux. Furthermore, as pointed out later, good spectroscopic performance is essential for measuring the polarization of the observed source photons as well as for improving the SNR by background rejection using Compton kinematics.

The geometric area of the required focal plane detector for a Laue lens mainly depends on the FOV provided by the Laue lens itself. In fact, as the point source shifts off axis, the PSF progressively broadens producing rings within a radius roughly proportional to the focal length. On the other hand, the detector thickness depends on the required detection efficiency in the operational energy band. From the current Laue lens development, it is realistic to infer a useful (i.e., with limited PSF degradation both in shape and in counts) Field of View of 3–4 arcmin. Assuming a focal length of 20 m, this implies lateral sizes for the focal plane detector smaller than 4 cm allowing for mapping the entire PSF. On the other hand, the requirement to be highly efficient (>80%) up to 600/700 keV, asks to increase the required sensitive volume of the detector up to 8/10 cm in all three dimensions, as recently evaluated by Monte Carlo simulation [45].
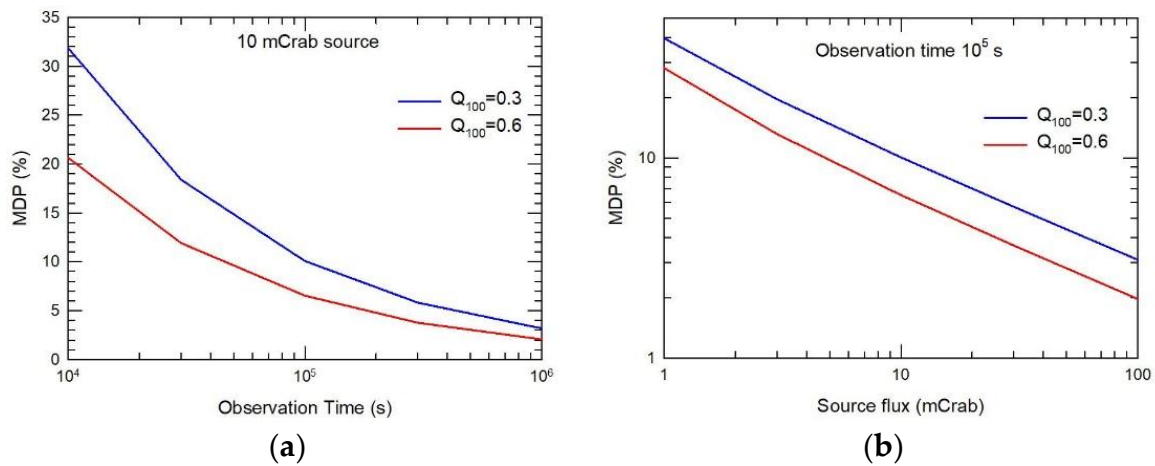

Figure 12. Polarimetric performance achievable by a 20 m focal length broadband (90–600 keV) Laue lens telescope with a fine (0.35 mm) spatial resolution focal plane in a LEO orbit: (**a**) Minimum Detectable polarization (MDP) vs observation time for a 10 mCrab source and two representative modulation factors ($Q_{100} = 0.3$ for all double events, $Q_{100} = 0.6$ for double events selected using both hits energy and coordinates to maximize the modulation factor); and, (**b**) MDP vs source intensity (100% polarized) for a 10^5 s observation time.

Assuming a focal plane detector with the required fine spatial resolution (0.35 mm) in the three dimensions, and a CZT sensitive volume of $10 \times 10 \times 10$ cm^3, we can evaluate the MDP achievable for a broadband Laue lens telescope with the characteristics reported in [35], in the 90–600 keV band in a Low Earth Orbit (LEO). For such type of instrument, in the MDP expression defined by Equation (4), the term giving the source counts ($A \cdot S_F$) is the product of the source flux (photons/s/cm^2) integrated over a defined energy band (ΔE) by the Laue lens collecting area in the same energy band. The coefficient B is the background in counts/s integrated over ΔE and on a surface (cm^2) described by the radius (FWHM) of the PSF, i.e., $\pi \cdot 3^2$ mm^2 (~0.3 cm^2). Using a source with a Crab spectrum [46], focal plane

detector double events efficiencies, as evaluated by Monte Carlo over the Laue lens pass band, and backgrounds level, as reported in [40], we could estimate the achievable MDP for different observation time and various source intensities. In the Figure 12 we used two values of the modulation factor Q_{100} derived from measurements with pixel CZT detectors described in Section 4 using an almost 100% polarized beam. These values are compatible with the assumed focal plane 3D spatial resolution of 0.35 mm in each direction. In fact, with the required 3D segmentation of the focal plane detector, we are confident to reach modulation factor very close to the expected theoretical values for each energy.

7. Conclusions

The possibility to operate 2D/3D CZT/CdTe spectrometers as Compton scattering detectors relies on the appealing opportunity to use these devices for hard x/γ-rays polarimetry. Today, this type of measurement is recognized for its fundamental importance in high-energy astrophysics and is one of the most demanding requirements for the next space mission instrumentation in this energy band (10–1000 keV). In this perspective, the development of high performance 3D spectrometers that are able to handle properly scattered events in three dimensions over the entire sensitive volume could represent a real breakthrough for a high demanding measurement, such as hard X- and γ-ray polarimetry. This development can definitely open the polarimetric dimension in hard X/γ-rays astronomy, making polarimetry the new standard observation mode in the next space instrumentation.

In the case of 3D spectrometer devices, each single sensor unit could be operated as a Compton detector, and therefore as a scattering polarimeter [24]. As seen, the quality (modulation factor) of a scattering polarimeter strictly depends on both spatial and spectroscopic resolution, because these parameters affect the capability of Compton kinematic reconstruction and good event selection [27,29]. When compared to the pixel detectors, the determination of the 3D position of each hit in scattering events represents a great advantage in the measurement of polarization as it allows for a more accurate reconstruction of the Compton kinematics, and therefore a more efficient selection of the events to optimize the response to the polarization modulation. For example, a better Compton kinematic reconstruction allows for implementing reliable methods to recognize good events (i.e., events form the source) with respect to chance coincidence ones and background events, thus improving the signal-to-noise ratio of the detection. The 3D spatial resolution capability can also help to handle some typical systematics that can negatively affect polarization measurements, such as the one introduced by incoming flux direction angle. Furthermore, the possibility to select events within thin layers of the sensitive volume, thanks to the 3D segmentation of the detector, could drastically improve the modulation factor, and therefore the reliability of the polarimetric measurements [40].

References

1. Lei, F.; Dean, A.J.; Hills, G.L. Compton Polarimetry in Gamma-Ray Astronomy. *Space Sci. Rev.* **1997**, *82*, 309–388. [CrossRef]
2. Bellazzini, R.; Costa, E.; Matt, G.; Tagliaferri, G. (Eds.) *X-ray Polarimetry: A New Window in Astrophysics*; Cambridge University Press: New York, NY, USA, 2010.
3. McConnell, M.; Matthew, G.B.; Bellazzini, R.; Bloser, P.F.; Costa, E.; Dennis, B.; Depaola, G.; Dovciak, M.; Elsner, R.; Emslie, A.G.; et al. X-ray and Gamma-Ray Polarimetry. Available online: http://research.sabanciuniv.edu/12371/ (accessed on 4 July 2018).

4.　Winkler, C.; Courvoisier, T.J.-L.; Di Cocco, G.; Gehrels, N.; Giménez, A.; Grebenev, S.; Hermsen, W.; Mas-Hesse, J.M.; Lebrun, F.; Lund, N.; et al. The Integral Mission. *Astron. Astrophys.* **2003**, *411*, L1–L6. [CrossRef]

5.　Dean, A.J.; Clark, D.J.; Stephen, J.B.; McBride, V.A.; Bassani, L.; Bazzano, A.; Bird, A.J.; Hill, A.B.; Shaw, S.E.; Ubertini, P. Polarized gamma ray emission from the CRAB. *Science* **2008**, *321*, 1183–1185. [CrossRef] [PubMed]

6.　Forot, M.; Laurent, P.; Grenier, I.A.; Gouiffès, C.; Lebrun, F. Polarization of the Crab Pulsar and Nebula as Observed by the INTEGRAL/IBIS Telescope. *Astrophys. J.* **2008**, *688*, L29. [CrossRef]

7.　Laurent, P.; Rodriguez, J.; Wilms, J.; Cadolle Bel, M.; Pottschmidt, K.; Grinber, V. Polarized Gamma-Ray Emission from the Galactic Black Hole Cygnus X-1. *Science* **2011**, *332*, 438–439. [CrossRef] [PubMed]

8.　Götz, D.; Laurent, P.; Lebrun, F.; Daigne, F.; Bošnjak, Ž. Variable polarization measured in the prompt emission of GRB 041219A using IBIS on board INTEGRAL. *Astrophys. J. Lett.* **2009**, *695*, L208.

9.　Yonetoku, D.; Murakami, T.; Gunji, S.; Mihara, T.; Toma, K.; Morihara, Y.; Takahashi, T.; Wakashima, Y.; Yonemochi, H.; Sakashita, T.; et al. Magnetic Structures in Gamma-Ray Burst Jets Probed by Gamma-Ray Polarization. *Astrophys. J. Lett.* **2012**, *758*, L1. [CrossRef]

10.　Rao, A.R.; Chand, V.; Hingar, M.K.; Iyyani, S.; Khanna, R.; Kutty, A.P.K.; Malkar, J.P.; Paul, D.; Bhalerao, V.B.; Bhattacharya, D.; et al. Astrosat CZT Imager Observations of GRB 151006A: Timing, Spectroscopy, and polarization Study. *Astrophys. J.* **2016**, *883*, 86. [CrossRef]

11.　Vadawale, S.V.; Chattopadhyay, T.; Mithun, N.P.S.; Rao, A.R.; Bhattacharya, D.; Vibhute, A.; Bhalerao, V.B.; Dewangan, G.C.; Misra, R.; Paul, B.; et al. Phase-resolved X-ray polarimetry of the Crab pulsar with the AstroSat CZT Imager. *Nat. Astron.* **2018**, *2*, 50–55. [CrossRef]

12.　Chauvin, M.; Florén, H.-G.; Friis, M.; Jackson, M.; Kamae, T.; Kataoka, J.; Kawano, T.; Kiss, M.; Mikhalev, V.; Mizuno, T.; et al. Shedding new light on the Crab with polarized X-rays. *Sci. Rep.* **2017**, *7*, 7816. [CrossRef] [PubMed]

13.　Kole, M.; Bao, T.W.; Batsch, T.; Bernasconi, T.; Cadoux, F.; Chai, J.Y.; Dong, Y.W.; Gauvin, N.; Hajdas, W.; He, J.J.; et al. POLAR: Final Calibration and In-Flight Performance of a Dedicated GRB Polarimeter. In Proceedings of the 2016 IEEE Nuclear Science Symposium, Medical Imaging Conference and Room-Temperature Semiconductor Detector Workshop (NSS/MIC/RTSD), Strasbourg, France, 29 October–6 November 2016; pp. 1–6.

14.　Chauvin, M.; Jackson, M.; Kawano, T.; Kiss, M.; Kole, M.; Mikhalev, V.; Moretti, E.; Takahashi, H.; Pearce, M. Optimising a balloon-borne polarimeter in the hard X-ray domain: From the PoGOLite Pathfinder to PoGO+. *Astrophys. Phys.* **2016**, *82*, 99–107. [CrossRef]

15.　Kislat, F.; Abarr, Q.; Beheshtipour, B.; De Geronimo, G.; Dowkontt, P.; Tang, J.; Krawczynski, H. Optimization of the design of X-Calibur for a long-duration balloon flight and results from a one-day test flight. *J. Astrophys. Telesc. Instrum. Syst.* **2018**, *4*, 011004. [CrossRef]

16.　Knödlseder, J.; von Ballmoos, P.; Frontera, F.; Bazzano, A.; Christensen, F.; Hernanz, M.; Wunderer, C. GRI: Focusing on the evolving violent universe. *Proc. SPIE* **2007**, *6688*, 668806.

17.　Von Ballmoos, P.; Takahashi, T.; Boggs, S.E. A DUAL mission for nuclear astrophysics. *Nucl. Instr. Meth. Phys. Res. A* **2010**, *623*, 431–433. [CrossRef]

18.　Tatischeff, V.; De Angelis, A.; Gouiffès, C.; Hanlon, L.; Laurent, P.; Madejski, G.M.; Tavani, M.; Ulyanov, A. e-ASTROGAM mission: A major step forward for gamma-ray polarimetry. *J. Astrophys. Telesc. Instrum. Syst.* **2018**, *4*, 011003.

19.　Caroli, E.; Bertuccio, G.; Cola, A.; da Silva, R.M.C.; Donati, A.; Dusi, W.; Landini, G.; Siffert, P.; Sampietro, M.; Stephen, J.B. Hard X-ray polarimetry with a thick CdTe position sensitive spectrometer. *Proc. SPIE* **2000**, *4140*, 573–584.

20.　Del Sordo, S.; Abbene, L.; Caroli, E.; Mancini, A.M.; Zappettini, A.; Ubertini, P. Progress in the Development of CdTe and CdZnTe Semiconductor Radiation Detectors for Astrophysical and Medical Applications. *Sensors* **2009**, *9*, 3491–3526. [CrossRef] [PubMed]

21.　Suffert, M.; Endt, P.M.; Hoogenboom, A.M. Polarization Measurements of Proton Capture Gamma Rays. *Physica* **1959**, *25*, 659–700. [CrossRef]

22.　Weisskopf, M.C.; Elsner, R.F.; Kaspi, V.M.; O'Dell, S.L.; Pavlov, G.G.; Ramsey, B.D. X-ray Polarimetry and Its Potential Use for Understanding Neutron Stars. In *Neutron Stars and Pulsars. Astrophysics and Space Science Library*; Becker, W., Ed.; Springer: Berlin, Germany, 2009; Volume 357.

23. Xu, D.; He, Z.; Lehner, C.E.; Zhang, F. 4π Compton imaging with single 3D position sensitive CdZnTe detector. *Proc. SPIE* **2004**, *5540*, 144–156.

24. Xu, D.; He, Z.; Zhang, F. Detection of gamma ray polarization using a 3-D position-sensitive CdZnTe detector. *IEEE Trans. Nucl. Sci.* **2005**, *52*, 1160–1164. [CrossRef]

25. Da Silva, R.M.C.; Auricchio, N.; Caroli, E.; Donati, A.; Hage-Ali, M.; Schiavone, F.; Siffert, P.; Stephen, J.B.; Ventura, G. Hard-X and soft gamma-ray polarimetry with CdTe array prototypes. *IEEE Trans. Nucl. Sci.* **2004**, *51*, 2478–2484. [CrossRef]

26. Da Silva, R.M.C.; Caroli, E.; Stephen, J.B.; Pisa, A.; Auricchio, N.; Del Sordo, S.; Frontera, F.; Honkimäki, V.; Schiavone, F.; Donati, A.; et al. Polarimetric performance of a Laue lens gamma ray CdZnTe focal plane prototype. *J. Appl. Phys.* **2008**, *104*, 084903. [CrossRef]

27. Caroli, E.; da Silva, R.M.C.; Stephen, J.B.; Pisa, A.; Auricchio, N.; Del Sordo, S.; Donati, A.; Schiavone, F.; Landini, G.; Honkimaki, V.; et al. A polarimetric experiment with a Laue Lens and CZT pixel detector. *IEEE Trans. Nucl. Sci.* **2009**, *56*, 1848–1854. [CrossRef]

28. Da Silva, R.M.C.; Auricchio, N.; Caroli, E.; Donati, A.; Del Sordo, S.; Honkimaki, V.; Maia, J.M.; Schiavone, F.; Stephen, J.B.; Trindade, A.; et al. Polarimetry study with a CdZnTe focal plane detector. *IEEE Trans. Nucl. Sci.* **2011**, *58*, 2118–2123. [CrossRef]

29. Da Silva, R.M.C.; Caroli, E.; Stephen, J.B.; Auricchio, N.; Maia, J.M.; Del Sordo, S.; Basili, A.; Schiavone, F.; Gloster, C.P.; Trindade, A.M.F.; et al. Polarization degree and direction angle effects on a CdZnTe focal plane performance. *IEEE Trans. Nucl. Sci.* **2012**, *59*, 1628–1635. [CrossRef]

30. Antier, S.; Ferrando, P.; Limousin, O.; Caroli, E.; da Silva, R.M.C.; Blondel, C.; Chipaux, R.; Honkimaki, V.; Horeau, B.; Laurent, P.; et al. Hard X-ray polarimetry with Caliste, a high performance CdTe based imaging spectrometer. *Exp. Astron.* **2015**, *39*, 233–258. [CrossRef]

31. Allison, J.; Amako, K.; Apostolakis, J.; Arce, P.; Asai, M.; Aso, T.; Bagli, E.; Bagulya, A.; Banerjee, S.; Barrand, G.; et al. Recent developments in GEANT4. *Nucl. Instr. Meth. Phys. Res. A* **2016**, *835*, 186–225. [CrossRef]

32. De Geronimo, G.; O'Connor, P.; Kandasamy, A.; Grosholz, J. Advanced-readout ASICs for multielement CdZnTe detectors. *Proc. SPIE* **2003**, *4784*, 105–119.

33. Limousin, O.; Lugiez, F.; Gevin, O.; Meuris, A.; Blondel, C.; Delagnes, E.; Donati, M.; Le Mer, I.; Martignac, J.; Pinsard, F.; et al. Caliste 256: A CdTe imaging spectrometer for space science with a 580 μm pixel pitch. *Nucl. Instr. Meth. Phys. Res. A* **2011**, *647*, 46–54. [CrossRef]

34. Ferrando, P.; Goldwurm, A.; Laurent, P.; Limousin, O.; Martignac, J.; Pinsard, F.; Rio, Y.; Roques, J.P.; Citterio, O.; Pareschi, G.; et al. SIMBOL-X: A formation-flying mission for hard X-ray astrophysics. *Proc. SPIE* **2005**, *5900*, 195. [CrossRef]

35. Gevin, O.; Lugiez, F.; Limousin, O.; Baron, P.; Blondel, C.; Coppolani, X.; Dirks, B.P.F.; Delagnes, E. IDeF-X V1.0: A new 16-channel low-noise analog front-end for Cd(Zn)Te detectors. *Nucl. Instr. Meth. Phys. Res. A* **2006**, *567*, 140–144. [CrossRef]

36. Vetter, K.; Burks, M.; Cork, C.; Cunningham, M.; Chivers, D.; Hulla, E.; Krings, T.; Manini, H.; Mihailescu, L.; Nelson, K.; et al. High-sensitivity Compton imaging with position-sensitive Si and Ge detectors. *Nucl. Instr. Meth. Phys. Res. A* **2007**, *579*, 363–366. [CrossRef]

37. Sato, G.; Hagino, K.; Watanabe, S.; Genba, K.; Atsushi, H.; Hironori, K.; Kataoka, J.; Katsuragawa, M.; Kawaharada, M.; Kobayashi, S.; et al. The Si/CdTe semiconductor camera of the ASTRO-H Hard X-ray Imager (HXI). *Nucl. Instr. Meth. Phys. Res. A* **2016**, *831*, 235–241. [CrossRef]

38. Zhang, F.; Herman, C.; He, Z.; De Geronimo, G.; Vernon, E.; Fried, J. Characterization of the H3D ASIC Readout System and 6.0 cm^3 3-D Position Sensitive CdZnTe Detectors. *IEEE Trans. Nucl. Sci.* **2012**, *59*, 236–242.

39. Kuvvetli, I.; Budtz-Jørgensen, C.; Zappettini, A.; Zambelli, N.; Benassi, G.; Kalemci, E.; Caroli, E.; Stephen, J.B.; Auricchio, N. A 3D CZT high resolution detector for x- and gamma-ray astronomy. *Proc. SPIE* **2014**, *9154*, 91540X.

40. Caroli, E.; De Cesare, G.; da Silva, R.M.C.; Abbene, L.; Auricchio, N.; Budtz-Jørgensen, C.; Del Sordo, S.; Ferrando, P.; Galvèz, J.L.; Hernanz, M.; et al. Monte Carlo evaluation of a CZT 3D spectrometer suitable for a Hard X- and soft-γ rays polarimetry balloon borne experiment. In Proceedings of the 2015 IEEE Nuclear Science Symposium and Medical Imaging Conference (NSS/MIC) Record, San Diego, CA, USA, 31 October–7 November 2015.

41. Harrison, F.; Craig, W.W.; Christensen, F.E.; Hailey, C.J.; Zhang, W.W.; Boggs, S.E.; Stern, D.; Cook, W.R.; Forster, K.; Giommi, P.; et al. The Nuclear Spectroscopic Telescope Array (NuSTAR) High-energy X-ray Mission. *Astrophys. J.* **2013**, *770*, 103. [CrossRef]

42. Frontera, F.; Virgilli, E.; Valsan, V.; Liccardo, V.; Carassiti, V.; Caroli, E.; Cassese, F.; Ferrari, C.; Guidi, V.; Mottini, S.; et al. Scientific prospects in soft gamma-ray astronomy enabled by the LAUE project. *Proc. SPIE* **2013**, *8861*, 886106.

43. Buffagni, E.; Bonnini, E.; Ferrari, C.; Virgilli, E.; Frontera, F. X-ray characterization of curved crystals for hard X-ray astronomy. *Proc. SPIE* **2015**, *9510*, 951006.

44. Virgilli, E.; Valsan, V.; Frontera, F.; Caroli, E.; Liccardo, V.; Stephen, J.B. Expected performances of a Laue lens made with bent crystals. *J. Astrophys. Telesc. Instrum. Syst.* **2017**, *3*, 044001. [CrossRef]

45. Khalil, M.; Frontera, F.; Caroli, E.; Virgilli, E.; Valsan, V. A simulation study on the focal plane detector of the LAUE project. *Nucl. Instr. Meth. Phys. Res. A* **2015**, *786*, 59–70. [CrossRef]

46. Kirsch, M.G.F.; Briel, U.G.; Burrows, D.; Campana, S.; Cusumano, G.; Ebisawa, K.; Freyberg, M.J.; Guainazzi, M.; Haberl, F.; Jahoda, K.; et al. Crab: The standard X-ray candle with all (modern) X-ray satellites. *Proc. SPIE* **2005**, *5898*, 589803.